Observations of Large-Scale Ocean–Atmosphere Interaction in the Southern Hemisphere

LAURA M. CIASTO AND DAVID W. J. THOMPSON

Department of Atmospheric Science, Colorado State University, Fort Collins, Colorado

(Manuscript received 11 December 2006, in final form 25 May 2007)

ABSTRACT

The authors provide a detailed examination of observed ocean–atmosphere interaction in the Southern Hemisphere (SH). Focus is placed on the observed relationships between variability in SH extratropical sea surface temperature (SST) anomalies, the Southern Annular Mode (SAM), and the El Niño–Southern Oscillation (ENSO). Results are examined separately for the warm (November–April) and cold (May–October) seasons and for monthly and weekly time scales. It is shown that the signatures of the SAM and ENSO in the SH SST field vary as a function of season, both in terms of their amplitudes and structures. The role of surface turbulent and Ekman heat fluxes in driving seasonal variations in the SAM- and ENSO-related SST anomalies is investigated. Analyses of weekly data reveal that variability in the SAM tends to precede anomalies in the SST field by ~1 week, and that the *e*-folding time scale of the SAM-related SST field anomalies is at least 4 months. The persistence of the SAM-related SST anomalies is consistent with the passive thermal response of the Southern Ocean to variations in the SAM, and seasonal variations in the persistence of the SAM-related SST anomalies are consistent with the seasonal cycle in the depth of the ocean mixed layer.

1. Introduction

Much of the existing literature on large-scale extratropical ocean–atmosphere interaction is focused on the North Atlantic and North Pacific sectors of the World Ocean, primarily because of the high quality and quantity of ocean observations in the extratropical Northern Hemisphere (NH) relative to the Southern Hemisphere (SH). For example, until the late 1970s–early 1980s, most sea surface temperature (SST) observations were measured in situ on board ships crossing between major population centers in North America, Europe, and Asia. Relative to the NH, the number of ships crossing the SH ocean basins is small, and thus there are fewer in situ SST observations in the Southern Ocean (e.g., Reynolds and Smith 1994).

Despite the lack of in situ SST data in the SH, satellite-derived SST data are available throughout the global ocean starting in the late 1970s–early 1980s. Hence, there are now several decades of satellite-derived SST observations available for the SH, a period long enough to warrant detailed explorations of large-scale SH ocean–atmosphere interaction. The purpose of this paper is to utilize the increasing array of SST observations available for the SH to provide a comprehensive summary of the relationships between large-scale climate variability and SH extratropical SST anomalies.

Large-scale atmospheric variability in the SH is dominated by two patterns of climate variability: the Southern Annular Mode (SAM) and the remote response to the El Niño–Southern Oscillation phenomenon (ENSO). The SAM is characterized by nearly zonally symmetric north–south vacillations in the latitude of the midlatitude atmospheric westerly jet (Kidson 1988; Karoly 1990; Thompson and Wallace 2000). The high index polarity of the SAM is defined as periods when the midlatitude jet is contracted poleward, and thus when the flow to the south of 50°S is anomalously westerly and pressures over the SH pole are anomalously low. The low index polarity of the SAM is defined by anomalies in the opposite sense. The SAM has a time scale of ~10 days (Lorenz and Hartmann 2001), is believed to reflect a positive feedback between the zonal flow and transient eddies in the SH storm track (Lorenz and Hartmann 2001), and explains

Corresponding author address: Laura M. Ciasto, Department of Atmospheric Science, Colorado State University, Fort Collins, CO 80523-1371.
E-mail: lciasto@atmos.colostate.edu

DOI: 10.1175/2007JCLI1809.1

~25% of the month-to-month variability in the SH geopotential height field (Kidson 1988; Karoly 1990; Thompson and Wallace 2000).

In contrast to the zonally symmetric structure of the SAM, the SH atmospheric response to ENSO is predominantly wavelike (e.g., Karoly 1989; Kiladis and Mo 1998; Kidson and Renwick 2002). During the warm phase of the ENSO cycle (i.e., El Niño conditions), increased convection in the central tropical Pacific creates anomalous upper-level vorticity, which is advected poleward in the upper tropical troposphere by the mean meridional circulation (Sardesmukh and Hoskins 1988). From the subtropics, the anomalous vorticity excites a pattern of standing Rossby waves extending from the subtropics toward North America in the NH and the Southern Ocean in the SH (Hoskins and Karoly 1981). In the SH, the wave train associated with the warm phase of ENSO is characterized by cyclonic anomalies to the west of New Zealand, anticyclonic anomalies to the west of the Antarctic Peninsula and cyclonic anomalies off the east coast of southern South America (Karoly 1989).

A complicating factor in interpreting large-scale SH atmospheric variability is that, during austral summer, the remote response to ENSO includes not only the wavelike response noted above but also a component that projects onto the SAM (L'Heureux and Thompson 2006). Thus, as discussed in the results, the impacts of the SAM and ENSO on high-latitude SH climate bear strong resemblance to each other during the SH summer season.

The impact of the SAM on variability in the extratropical SH SST field has been examined in only a handful of observational and modeling studies (e.g., Watterson 2000; Hall and Visbeck 2002; Holland et al. 2005; Lovenduski and Gruber 2005; Verdy et al. 2006; Sen Gupta and England 2006). Observations reveal the pattern of SST anomalies associated with the high index polarity of the SAM is marked by predominantly warm SST anomalies along 30°–40°S, cold SST anomalies along 50°–60°S, and a broad region of enhanced cold SST anomalies in the Southern Ocean centered near 50°S, 130°W (Lovenduski and Gruber 2005; Sen Gupta and England 2006). Numerical results reveal a qualitatively similar impact of the SAM on the SST field (e.g., Hall and Visbeck 2002; Holland et al. 2005; Sen Gupta and England 2006), though in general the climate model ocean response to the SAM is more zonally symmetric than the observations (e.g., Hall and Visbeck 2002). Verdy et al. (2006) note a large fraction of SST variability in the vicinity of the Antarctic Circumpolar Current (ACC) is consistent with surface turbulent and Ekman heat fluxes associated with variability in the SAM as well as ENSO. Meredith et al. (2004) argue the SAM impacts ocean transport through the Drake Passage and Meredith and Hogg (2006) reveal the SAM drives anomalies in kinetic energy in the ACC. Lefebvre et al. (2004) demonstrate that the SAM influences the distribution of sea ice around Antarctica.

The pattern of SST anomalies associated with the SH extratropical response to ENSO has also been documented in a select number of observational and modeling studies (e.g., Li 2000; Renwick 2002; Kidson and Renwick 2002; Holland et al. 2005; Verdy et al. 2006). The SH SST response to ENSO is associated primarily with a dipole in SST anomalies between the region to the north of New Zealand and near the region centered near 50°S, 140°W. The pattern of SST anomalies associated with ENSO is similar to the leading empirical orthogonal function (EOF) of extratropical SH SST anomalies (Kidson and Renwick 2002).

The goal of the present study is to provide a comprehensive summary of the observed relationships between large-scale SH atmospheric variability and the SH extratropical SST field. The study supports findings published in the aforementioned studies but also extends previous work by 1) examining seasonal variations in the patterns of SSTs associated with the SAM and ENSO, 2) explicitly comparing and contrasting the SST patterns associated with the SAM and ENSO, 3) providing a more detailed analysis of the physical processes that drive observed SST anomalies throughout the SH middle and high latitudes, 4) using weekly data to examine lagged relationships between the SAM and the extratropical SST field, and 5) examining in detail the persistence of the SAM-related SST anomalies. The rest of the paper is outlined as follows: section 2 summarizes the data and methods. In section 3, we examine contemporaneous relationships between ENSO and the SAM and monthly-mean SST anomalies, and also explore the physical processes that generate the observed SST anomalies. Section 4 documents the temporal evolution of the relationships between the SAM and extratropical SST anomalies on weekly time scales and offers an interpretation of the persistence of the SAM-related SST anomalies. Section 5 provides a summary and discussion of the results.

2. Data and methods

The primary data used in the study are monthly and weekly-mean values of optimally interpolated (OI) sea surface temperatures from the NOAA_OI_SST_V2 dataset (hereafter referred to as the OI SST data). The SST data are provided by the National Oceanic and Atmospheric Administration (NOAA)/Office of Oce-

anic and Atmospheric Research (OAR)/Earth System Research Laboratory (ERSL), Boulder, Colorado, from their Web site at http://www.cdc.noaa.gov/. The OI SST data were derived from a blended objective analysis of both in situ and satellite observations and were smoothed with a three-point binomial filter applied in both time and space (Reynolds et al. 2002). The OI SST data are available on a 1° × 1° latitude–longitude grid from 1981 to 2005, but the true resolution of the data is closer to 6° × 6°, as discussed in O'Neill et al. (2003). We also use monthly SST data obtained from the Comprehensive Ocean–Atmosphere Dataset (COADS), which corresponds to a collection of surface observations gathered from merchant ships and buoys (Woodruff et al. 1987). The COADS data are available on a 2° × 2° latitude–longitude grid for the period 1900–2002.

Mixed layer depth data were obtained from the Ocean Mixed Layer Depth Climatology dataset (more information is available online at www.lodyc.jussieu.fr/~cdblod/mld.html), as described in de Boyer Montégut et al. (2004). The data are available in monthly-mean format on a 2° × 2° latitude–longitude mesh, and were derived from over four million individual vertical profiles taken between 1941 and 2002, which are archived by the National Oceanographic Data Center (NODC) and the World Ocean Circulation Experiment (WOCE). The depth of the mixed layer is defined as the depth at which the temperature differs from the temperature at 10 m by 0.2°C.

All atmospheric data are from the National Centers for Environmental Prediction–National Center for Atmospheric Research (NCEP–NCAR) reanalysis (Kistler et al. 2001) available from the NOAA/OAR/ESRL Physical Sciences Division (PSD). The NCEP/NCAR reanalysis data are gridded on a 2.5° × 2.5° latitude–longitude mesh and are used here in both monthly and daily format. Because of the temporal limitations of the OI SST record, we use the reanalysis data only for the period 1981–2005. Anomalies are defined as data in which the seasonal cycle has been removed. The seasonal cycle is removed from weekly (monthly) data by subtracting the long-term weekly (monthly) mean from each week (month) at each grid point.

The SAM and ENSO indices were obtained from the NOAA Climate Prediction Center (CPC). Daily-(monthly-) mean values of the SAM index are found by projecting daily (monthly) 700-mb height anomalies poleward of 20°S onto the leading empirical orthogonal function of monthly-mean 700-mb heights, calculated for the period 1979–2000. As noted in the introduction, the high index polarity of the SAM is characterized by negative height anomalies over the pole surrounded by positive height anomalies between 40° and 50°S. Monthly-mean variability in ENSO is defined on the basis of SST anomalies averaged over the region 5°S–5°N, 170°–120°W. The resulting cold-tongue index (CTI) is inverted such that positive values of the index correspond to the cold phase of the ENSO cycle, and vice versa. Before all analyses, the SAM and ENSO indices are standardized by subtracting the long-term means and dividing by the long-term standard deviations of the respective analysis periods.

The primary statistical tools used in the study are regression, correlation and principal component (PC) analysis (also referred to as EOF analysis). The statistical significance of all correlation coefficients is assessed using the t statistic in which the effective sample size, N_{eff}, is estimated as

$$N_{\text{eff}} = N\left[\frac{1 - r_1 r_2}{1 + r_1 r_2}\right], \tag{1}$$

where N is the sample size and r_1 and r_2 are the lag 1 autocorrelations of the two time series being correlated (Bretherton et al. 1999). The PC analyses are based on the temporal covariance matrix and are calculated for data first weighted by the square root of the cosine of latitude. The results are displayed as regressions of the unweighted monthly-mean data onto the standardized PC time series. Note the resulting regression maps are very similar but not identical to the EOFs, since the latter lie in cosine-weighted space. The significance of the EOF/PCs is estimated using the criteria outlined in North et al. (1982).

3. Southern Hemisphere ocean–atmosphere interaction on monthly time scales

a. Relevant aspects of the climatology

Before investigating the relationships between large-scale patterns of SH climate variability and the extratropical SST field, it is worth reviewing key climatological features of the SH ocean basins. The contours in the left and right panels of Fig. 1 show climatological seasonal-mean SSTs for the austral warm (November–April) and cold (May–October) seasons, respectively. During both times of year, the isotherms are nearly zonally symmetric, with SSTs decreasing monotonically toward the South Pole. Over most of the SH, the meridional gradients in SSTs are on the order of 4–5 K per 10° of latitude and exhibit a weak seasonal cycle. The meridional gradients in SST are enhanced in the region of the Agulhas Current, where they are as large as 8–10 K per 10° of latitude.

The shading in Fig. 1 shows the standard deviation of monthly-mean SST anomalies. The two most obvious

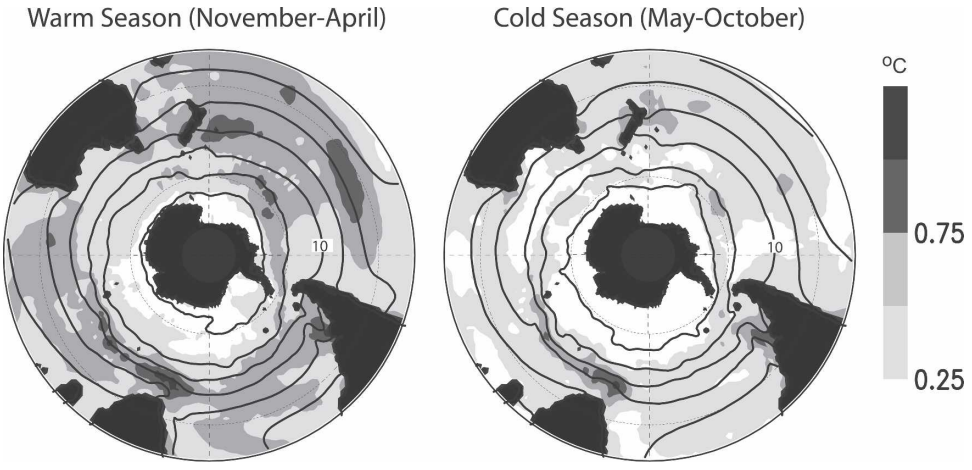

FIG. 1. Climatological mean SSTs (contours) and std dev of SST anomalies (shading) for the (left) warm and (right) cold seasons. Contour intervals are drawn at (0°, 5°, 10°C. . .). The 10°C contour is labeled.

features in the rms variance field are 1) the region of enhanced variance off the tip of South Africa in the vicinity of the Agulhas Current and 2) the ~0.5 K increase in rms variance throughout most of the SH oceans during the warm season. The region of locally enhanced variance associated with the Agulhas Current is analogous to regions of increased variance found in the vicinity of the Gulf Stream and Kuroshio in the Northern Hemisphere.

Figure 2 shows the climatological mean depth of the mixed layer for the warm and cold seasons (shading) superposed on the mean bounds on the location of the ACC (contours). The mean bounds on the position of the ACC are derived from Karsten and Marshall (2002), and correspond to the northernmost and southernmost lines of constant sea surface height (SSH) that encircle the globe uninterrupted by land [the SSH data are derived from Ocean Topography Experiment (TOPEX)/Poseidon altimetry data].

During the warm season, the mixed layer is on average less than 50 m deep equatorward of 45°S and between 50 and 100 m deep poleward of 45°S. The relatively shallow mixed layer depths during the summer are consistent with weaker convective and mechanical mixing during that season. The mixed layer is generally considerably deeper during the cold season, as vertical mixing in the upper layers of the ocean is enhanced. The increase in mixed layer depths during the cold season is most pronounced poleward of 45°S with the most extensive increases in mixed layer depths found just

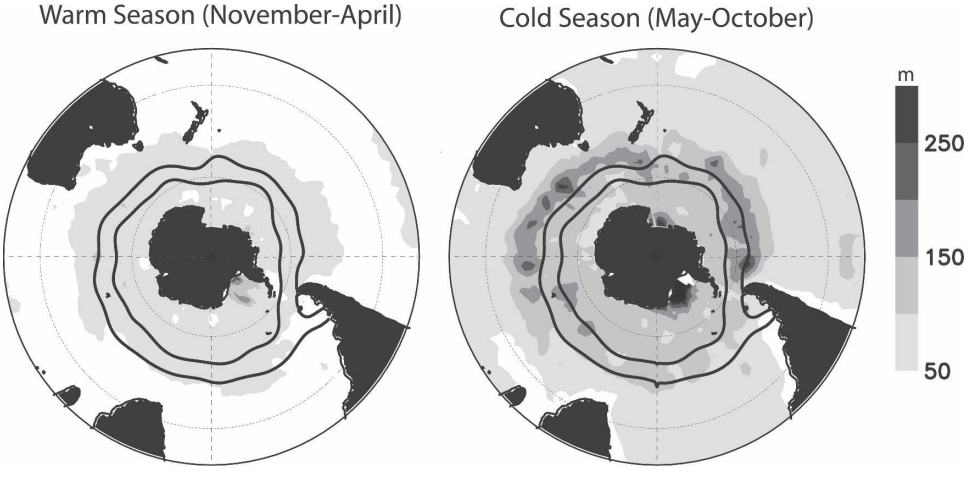

FIG. 2. Climatological mean mixed layer depths (shading) for the (left) warm and (right) cold seasons. Contours represent the mean path of ACC (see text for details of ACC).

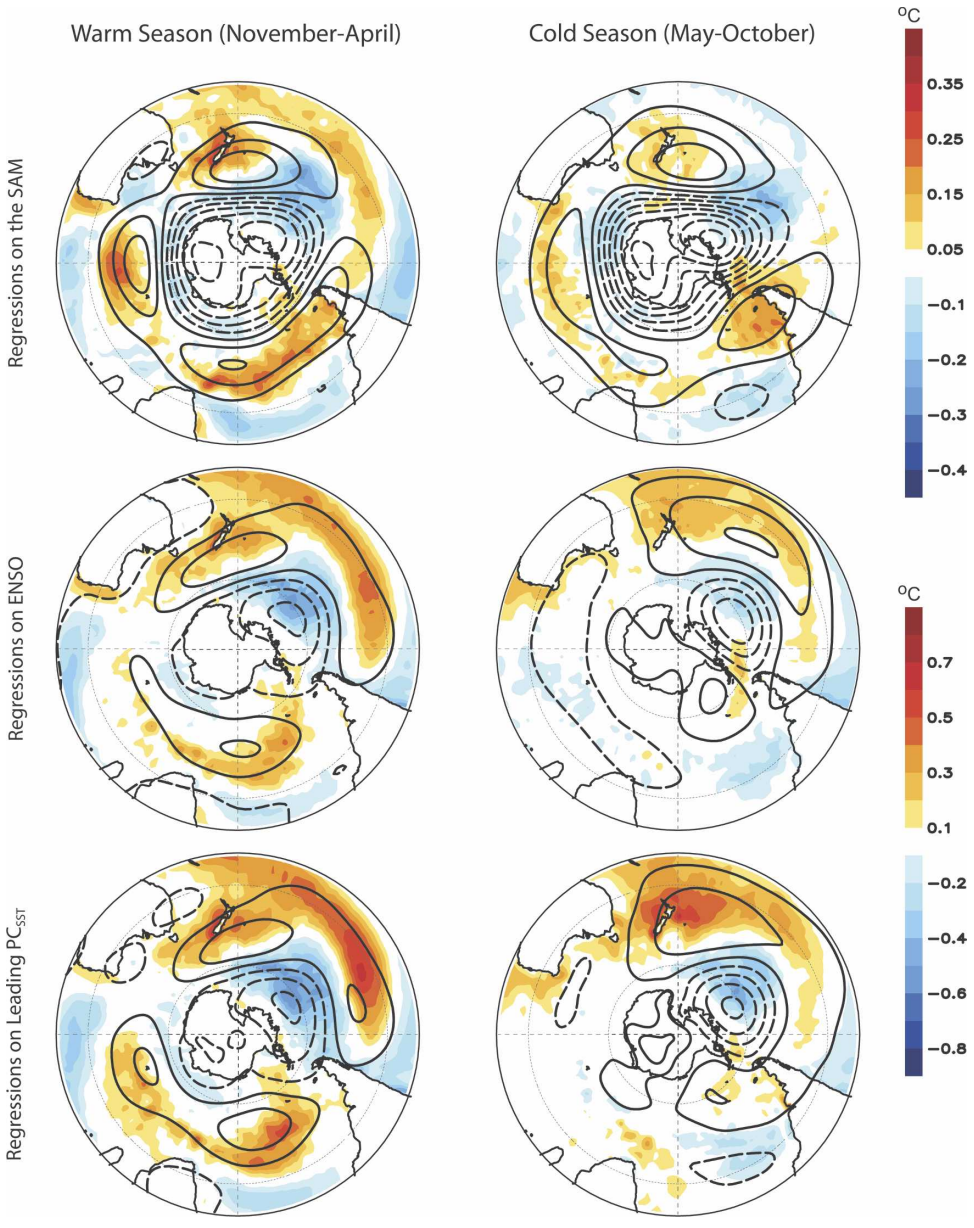

FIG. 3. Monthly-mean SST (shaded) and Z_{500} (contours) anomalies regressed onto the (top row) SAM index, (middle row) ENSO index, and (bottom row) leading principal component time series of monthly-mean SST anomalies. Positive (negative) contours are denoted by solid (dashed) lines and are drawn at (−5, 5, 15 m . . .). (left) Warm season (November–April) and (right) cold season (May–October) results. Note that the sign of the results corresponds to the high index polarity of the SAM and the cold phase of the ENSO cycle.

equatorward of the ACC from the central Indian Ocean (90°W) to the tip of South America. The mixed layer deepens considerably during winter in the Weddell Sea, consistent with enhanced deep-water formation in that region. Note that, for the most part, the winter season is associated with deeper mixed layers (Fig. 2) but lower standard deviations in the SST field (Fig. 1).

b. *Patterns of SH SST anomalies associated with the SAM and ENSO*

In this section, we investigate the structures of SST variability associated with the two most important patterns of SH climate variability: the SAM and the remote SH response to ENSO.

Maps formed by regressing monthly-mean SST and

500-hPa height (Z_{500}) anomalies onto standardized values of the SAM and ENSO indices are shown in the top and middle rows of Fig. 3, respectively. Contours (shading) correspond to Z_{500} (SST) anomalies. The left (right) panel corresponds to the warm (cold) season. Recall from section 2 that positive values of the ENSO index denote cold conditions in the eastern tropical Pacific, and vice versa. Thus, the anomalies in the regression maps correspond to the high index polarity of the SAM and the cold phase of the ENSO cycle.

As reviewed in the introduction, the high index polarity of the SAM is characterized by lower-than-normal heights over the polar regions and higher-than-normal heights ~40°S (contours, top panels). The structure of the SAM in Z_{500} is nearly identical throughout the year, but has a more pronounced trough to the west of the Antarctic Peninsula during the cold season. As also reviewed in the introduction, the structure of ENSO in Z_{500} has a stronger wavelike component than the SAM (contours, middle panels): during austral winter, the cold phase of the ENSO cycle is associated with positive height anomalies to the east of New Zealand, negative height anomalies to the west of the Antarctic Peninsula, and positive height anomalies in the Atlantic sector of the Southern Ocean. As noted in L'Heureux and Thompson (2006), during austral summer the SH response to ENSO also exhibits negative geopotential height anomalies that extend across the pole, and thus the signature of ENSO in Z_{500} field bears resemblance to the structure of the SAM (i.e., compare the contours in the top-left and middle-left panels). The correlation between monthly-mean indices of the SAM and ENSO is $r \sim 0.5$ during the months November–April (L'Heureux and Thompson 2006).

During the SH warm season, the similarities between the structure of the SAM and ENSO in the SH geopotential height field extend to the sea surface temperature field. For example, both the SAM and ENSO are associated with a broad region of negative SST anomalies in the South Pacific sector around 40°–60°S, 90°–150°W, positive SST anomalies centered around New Zealand and stretching from Australia to South America along 30°–40°S, positive SST anomalies along 45°S in the southern Atlantic Ocean, and negative SST anomalies along 20°–30°S in the eastern Pacific, Atlantic, and Indian Ocean basins. The spatial correlation between the SST regressions maps in the top-left and middle-left panels is ~0.75.

The most notable differences between the warm season ENSO and SAM SST regression maps lie in their amplitudes: the SAM-related SST anomalies are about half the amplitude of the ENSO-related SST anomalies (note the color scales for the ENSO and SAM regression maps are different). The differences in amplitudes between the ENSO and SAM SST regression maps are consistent with the relative time scales of SH SSTs and the SAM and ENSO indices used in the regressions; that is, most of the variance in the SAM index is found on month-to-month time scales, whereas much of the variance in both the ENSO index and Southern Ocean SSTs is found on interannual time scales. The amplitudes of the SAM and ENSO warm season regression maps are very similar when the SAM regression map is based on standardized seasonal-mean values of the SAM index (not shown).

During the SH cold season, fluctuations in ENSO are not significantly correlated with temporal variability in the SAM (L'Heureux and Thompson 2006). Thus the cold season SST regression maps (top- and middle-right panels of Fig. 3) may be viewed as more distinct expressions of the SAM and ENSO in the SH SST field. The cold season SAM regression map (top right) is similar to its warm season counterpart (top left) at middle and high latitudes but does not exhibit pronounced anomalies extending into the subtropical sector of the South Pacific. The cold season ENSO regression map (middle right) resembles its warm season counterpart (middle left) but does not exhibit substantial anomalies in the southern Atlantic and Indian Oceans. For the most part, SST anomalies associated with both the SAM and ENSO exhibit weaker amplitudes during the cold season than during the warm season. The cold season SAM regression map in the top-right panel is nearly identical to the pattern of SSTs associated with the SAM found for year-round data, as presented in Lovenduski and Gruber (2005) and Sen Gupta and England (2006).

How do the patterns of SST anomalies associated with the SAM and ENSO relate to the dominant structures of hemispheric-scale SH SST variability? The bottom panels in Fig. 3 show the regressions of monthly-mean SST (shading) and Z_{500} anomalies onto the standardized leading PC time series of the SST field calculated for the domain 20°–70°S. The patterns of SST variability associated with leading PC time series of the cold (right panel) and warm (left panel) seasons account for 15% and 13% of the total variance, respectively. The patterns of SST anomalies associated with the second PC (not shown) explain approximately 8% of the total variance in each season, and the leading EOF/PCs are well separated according to the criteria outlined in North et al. (1982).

As evidenced in Fig. 3 and quantified in Table 1, during both seasons the leading patterns of SH SST

TABLE 1. Correlation coefficients between the leading PCs of the SH SST field and the expansion coefficient time series for the SAM (top) and ENSO (bottom) SST regression maps from the top panels of Fig. 3. Left (right) column corresponds to cold (warm) season. See text for details.

	Leading PC time series (cold season)	Leading PC time series (warm season)
SAM-based regression	0.55	0.91
ENSO-based regression	0.93	0.99

variability project most strongly onto the pattern of SST anomalies associated with ENSO. Similarly, the patterns of Z_{500} anomalies associated with the leading PCs of SH SST variability (contours, bottom panels) bear strong resemblance to the structure of ENSO in the SH geopotential height field (contours, middle panels). The expansion coefficient time series of the ENSO SST regression maps in the middle panels are correlated with the leading PC time series of the SH SST field at a level of $r = 0.93$ during the cold season and $r = 0.99$ during the warm season (Table 1). Note that, during the warm season, the pattern of SST anomalies associated with the leading PC time series of SH SST anomalies also resembles the pattern of SST anomalies associated with the SAM by virtue of the correlation between the SAM and ENSO.

The results in Fig. 3 are based on SST anomalies obtained from the OI SST data, a blended analysis of satellite and in situ observations (Reynolds et al. 2002). The above analyses were repeated using SST data derived only from in situ observations obtained from COADS. The results based on the COADS data are noisy compared to those based on the OI SST data because of the sparse nature of in situ data over the Southern Ocean. However, the principle features evident in the SST patterns in Fig. 3 are reproducible over regions where in situ data are available (results not shown).

c. *Processes that drive SH SST variability on monthly time scales*

Below we examine the processes through which the SAM and ENSO give rise to the extratropical SST anomalies revealed in the previous section.

On the basis of previous research, we expect that the SAM and ENSO will impact extratropical SSTs predominantly through changes in surface turbulent fluxes of latent and sensible heat as well as heat advection from Ekman currents (e.g., Frankignoul and Hasselman 1977; Frankignoul 1985; Verdy et al. 2006; Sen Gupta and England 2006). Below we examine the seasonally varying relationships between the SAM and ENSO and the surface turbulent and Ekman heat fluxes, and compare the results with the patterns of SST anomalies shown in the previous section. The results are consistent with observational findings reported in Verdy et al. (2006), but we more explicitly compare the flux estimates with the pattern of SST anomalies associated with the SAM and ENSO, focus on regions outside the ACC, and highlight seasonally varying aspects of the relationships.

The top panels in Fig. 4 are a reproduction of the SST and Z_{500} anomalies from the top panels in Fig. 3. The middle and bottom two panels in Fig. 4 show the total surface turbulent heat fluxes (defined as the sum of the latent and sensible heat fluxes) and heat advection by the anomalous Ekman currents (hereafter referred to as the Ekman heat fluxes) regressed onto standardized values of the SAM index, respectively, for the SH warm (left) and cold (right) seasons. The contours are a reproduction of the Z_{500} height anomalies from the top panels. Positive values denote fluxes of heat into the ocean, and vice versa.

During both the warm and cold seasons, the high index polarity of the SAM is associated with positive surface turbulent heat fluxes (from the atmosphere to the ocean) throughout much of the zonal ring spanning 40°–50°S, with maximum positive flux anomalies centered around New Zealand and across a broad region extending eastward from the southern tip of South America to the Indian Ocean. The largest negative anomalies in the turbulent fluxes of heat (i.e., fluxes from the ocean to the atmosphere) are found during the cold season along 60°S, with substantial negative anomalies evident in the Pacific sector of the Southern Ocean between 40°–60°S and 100°–140°W.

The patterns of turbulent heat flux anomalies associated with the SAM index are consistent with the associated changes in the overlying flow. Bearing in mind that the large-scale atmospheric flow in the SH is close to geostrophic balance, and thus that the overlying Z_{500} anomalies approximate the direction of the anomalous atmospheric winds, we find the following. The regions of negative air-to-sea fluxes off the coast of east Antarctica and to the east of the Antarctic Peninsula are consistent with enhanced surface wind speeds in the latitude band of approximately 50°–60°S, the widespread positive air-to-sea fluxes of heat in SH middle latitudes are consistent with decreased surface wind speeds between 30° and 40°S, the band of locally enhanced negative air-to-sea fluxes near 40°–60°S, 100°–140°W in the Southern Ocean are coincident with anomalous southerly advection there, and the enhanced positive fluxes in the vicinity of the Drake Pas-

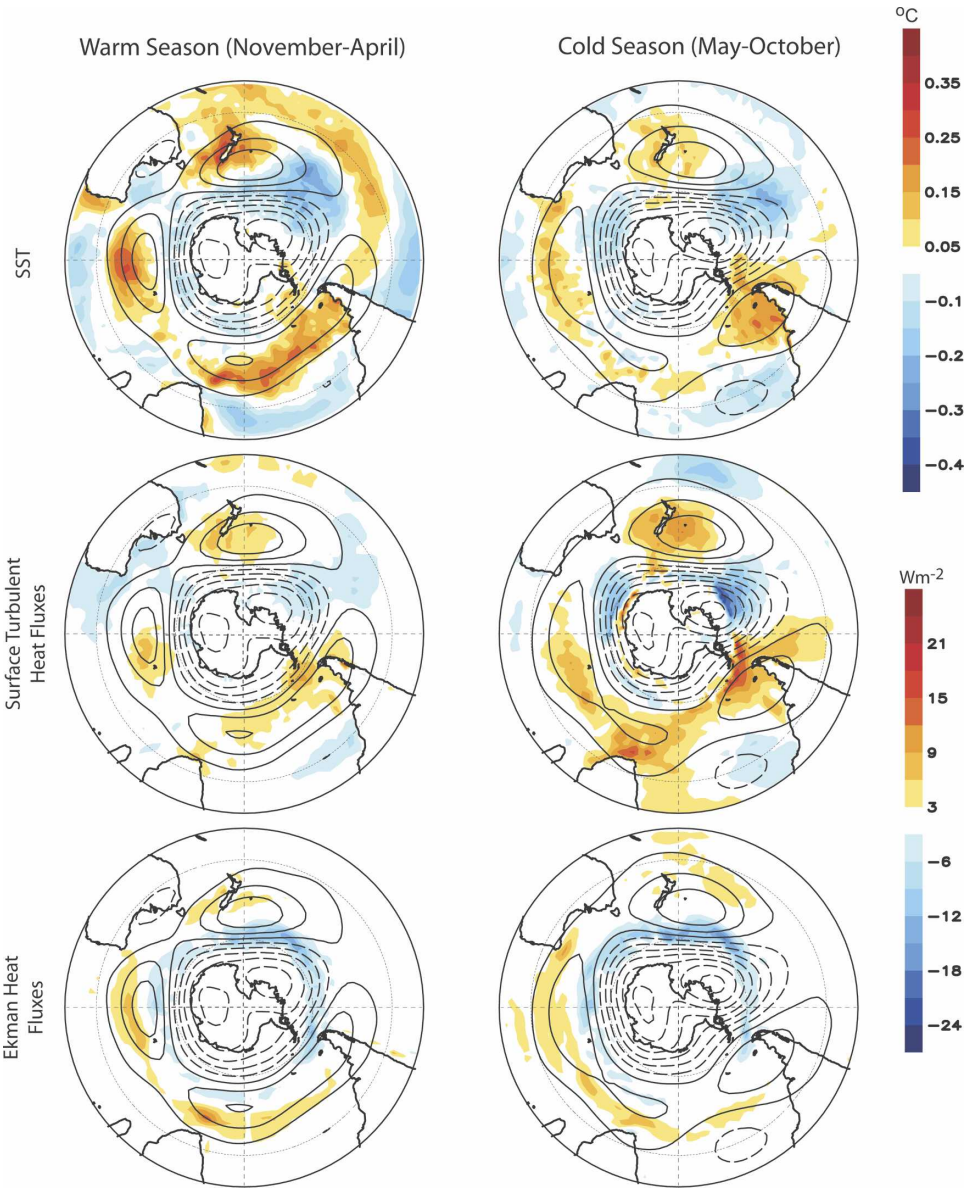

FIG. 4. Regressions of monthly-mean (all panels; contours) Z_{500}, (top; shading) SST, (middle; shading) surface turbulent heat flux, and (bottom; shading) Ekman heat flux anomalies regressed onto the SAM index. Positive (negative) contours correspond to solid (dashed) lines and are drawn at (−5, 5, 15 m . . .). (left) Warm season (November–April) and (right) cold season (May–October) results. The positive heat fluxes are directed into the ocean and are in W m^{-2}.

sage are consistent with anomalous northerly advection there.

The shading in the bottom panels of Fig. 4 shows the corresponding regressions for heat advection due to the anomalous Ekman currents. Consistent with findings reported by Verdy et al. (2006) for year-round data, negative Ekman heat flux anomalies are observed in much of the circumpolar region around 50°–60°S, but positive Ekman heat flux anomalies are also evident further north around 30°–40°S. The Ekman heat flux patterns are consistent with the anomalous Ekman currents inferred from the pattern of wind anomalies associated with the SAM; that is, the anomalous wind stress on the surface layers of the ocean drives anomalous northward Ekman transport along ~60°S but anomalous southward Ekman transport at 40°S.

The patterns of turbulent and Ekman heat flux anomalies associated with the SAM are similar in both SH cold and warm seasons but for one notable difference: the amplitude of the turbulent heat flux anoma-

lies (middle panels) are uniformly stronger during the SH cold season than they are during the warm season, whereas the amplitude of the Ekman heat fluxes (bottom panels) are comparable during both seasons. The weaker seasonal cycle in the Ekman heat fluxes is consistent with the weak seasonal cycles in the amplitude of the SAM and the meridional gradients in SSTs.

Comparing the flux regressions from the lower four panels in Fig. 4 with the top panels, it is evident that both the anomalous turbulent and Ekman heat fluxes play a substantial role in generating the extratropical SST anomalies associated with the SAM. Both the turbulent heat flux and SST maps exhibit positive anomalies at 40°–50°S throughout the South Atlantic, Indian, and western Pacific Oceans and negative anomalies in the central Pacific around 40°–60°S, 90°–140°W. The Ekman heat flux anomalies contribute most to the observed SST anomalies in the high-latitude Southern Ocean, as emphasized in Verdy et al. (2006), but also reinforce the positive turbulent heat flux anomalies along 40°S.

It is interesting that the amplitudes of the SST anomalies associated with the SAM are weakest during the cold season (top panels), but that the amplitudes of the attendant turbulent heat flux anomalies are largest during the cold season (middle panels). At first, these results seem counterintuitive since the SST anomalies associated with the SAM are presumably driven by, and hence are proportional to, the amplitude of the sensible and latent heat fluxes. However, as reviewed in Frankignoul (1985), the thermal inertia of the mixed layer is directly proportional to its depth, and thus the response of the SST field to anomalous turbulent heat fluxes is directly proportional to the amplitude of the fluxes but inversely proportional to the depth of the mixed layer. Hence, the presence of weaker SST anomalies during the cold season despite a ~50% increase in the heat fluxes is consistent with the roughly fourfold increases in SH wintertime mixed layer depths, as shown in Fig. 2.

Figure 5 is analogous to Fig. 4, but shows regressions based on the ENSO index (note that the color scales have changed from Fig. 4). The main features in the Ekman heat flux regressions (bottom panels) are evident in the SST anomalies (top panels); for example, the negative Ekman heat flux anomalies in the Pacific sector of the SH are consistent with the negative SST anomalies in that region; and the positive Ekman heat flux anomalies during the warm season south of Australia (40°S, 120°–180°E) and South Africa (40°S, 15°W–45°E) are also mirrored in the SST field. However, the resemblance between the ENSO turbulent heat flux and SST regression maps is less clear. During the cold season, the main features in the turbulent flux regression map are mirrored in the SST regression map, particularly over the Pacific sector of the hemisphere. But during the warm season the turbulent flux regression map exhibits features that are not evident in the SST field. In general, the similarities between the patterns of turbulent heat flux and SST anomalies are weaker for ENSO than they are for the SAM.

It is not clear why the patterns of anomalous turbulent heat fluxes associated with ENSO do not project strongly onto the patterns of ENSO-related SST anomalies. We repeated the analyses in Fig. 5 for seasonal mean data (to minimize the impact on the regressions of intraseasonal variability not related to ENSO), for data lagged by up to three months (to account for the fact that the atmospheric response to ENSO may lag tropical SST anomalies by several months), and for turbulent flux data from three different—though not entirely independent—flux data sources: the NCEP Reanalysis 2 data, which is an updated version of the NCEP reanalysis data used here; the 40-yr European Centre for Medium-Range Weather Forecasts (ECMWF) Re-Analysis (ERA-40) flux data; and the Woods Hole Oceanographic Institute Objectively Analyzed Air–Sea Flux Data. In all cases, the resulting flux regressions are qualitatively similar to the results in Fig. 5, which suggests the discrepancies between the middle and top panels of Fig. 5 transcends the specifics of the analysis procedure.

4. Relationships between the SAM and SST anomalies on weekly time scales

The previous section revealed the patterns of extratropical SST variability associated with the SAM and ENSO based on contemporaneous regressions using monthly-mean data. In this section, we investigate the temporal evolution of the relationships using weekly-mean data. Because ENSO variability is strongest on seasonal time scales, the following analyses of weekly data focus on the lagged relationships between extratropical SH SST anomalies and the SAM.

To examine the temporal evolution of the relationships between the SAM and the SST field, we use lagged correlation–regression analysis between weekly values of SST anomalies and the SAM index. Results are based on the 26-week cold (warm) season extending from the first week of May (November) to the last week in October (April). The regressions/correlations are centered about the middle 10 weeks of each season and are lagged from −8 (SST leads) to +8 (SST lags) weeks.

Figure 6 shows maps formed by regressing weekly-mean SST anomalies onto standardized values of the SAM index at lags ranging from −8 (top row) to +8

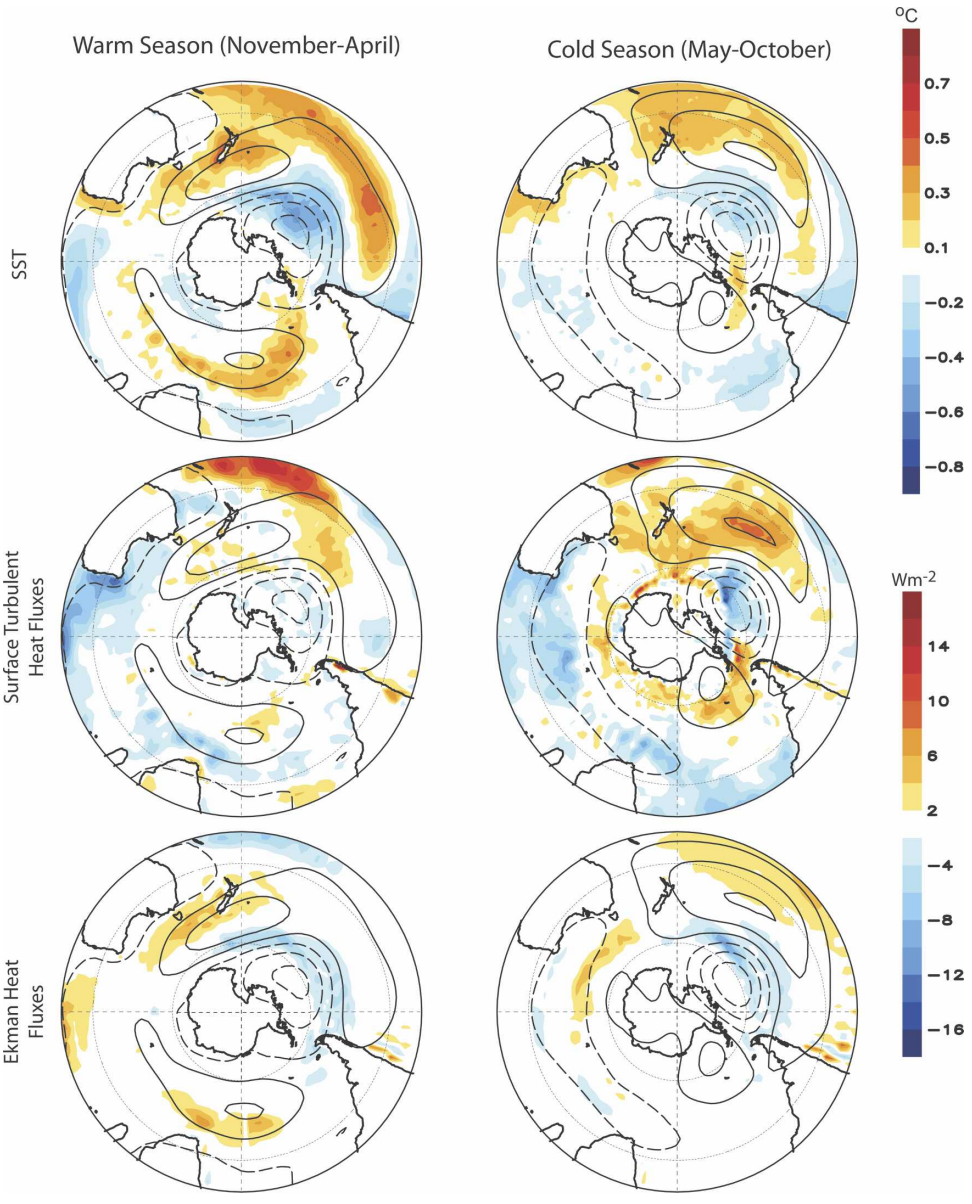

FIG. 5. As in Fig. 4, but the regressions are based on the standardized ENSO index. Positive values of the ENSO index denote cold conditions in the eastern tropical Pacific. Note that the color scales have changed from Fig. 4.

(bottom row) weeks for the warm (left) and cold (right) seasons. During both seasons, the SST anomalies exhibit patterns similar to the contemporaneous monthly-mean regression maps shown in the top panels of Fig. 3. The weekly regression maps exhibit similar structure at all lags, but have largest amplitude following lag 0. As is the case for the monthly regressions, the amplitudes of the SST anomalies are somewhat higher during the warm season (note the color scales for the warm and cold season regression maps in Fig. 6 are different).

Figure 7 shows the lag correlations between the SAM index and the expansion coefficient time series of the lag 0 SST maps in Fig. 6. The expansion coefficient time series (hereafter SAM_{SST}) were formed by projecting the anomalous weekly-mean SST field onto the lag 0 regression maps from Fig. 6. In practice, quantitatively similar time series are derived by projecting the SST field onto regression maps for other lags. During both the warm and cold seasons, the lag correlations between the SAM and its associated SST pattern are largest and most significant when variations in the SAM precede variations in the SST field by ~1 week, at which time $r \sim 0.45$. The lag correlations exhibit a marked asymmetry about lag 0; for example, the cor-

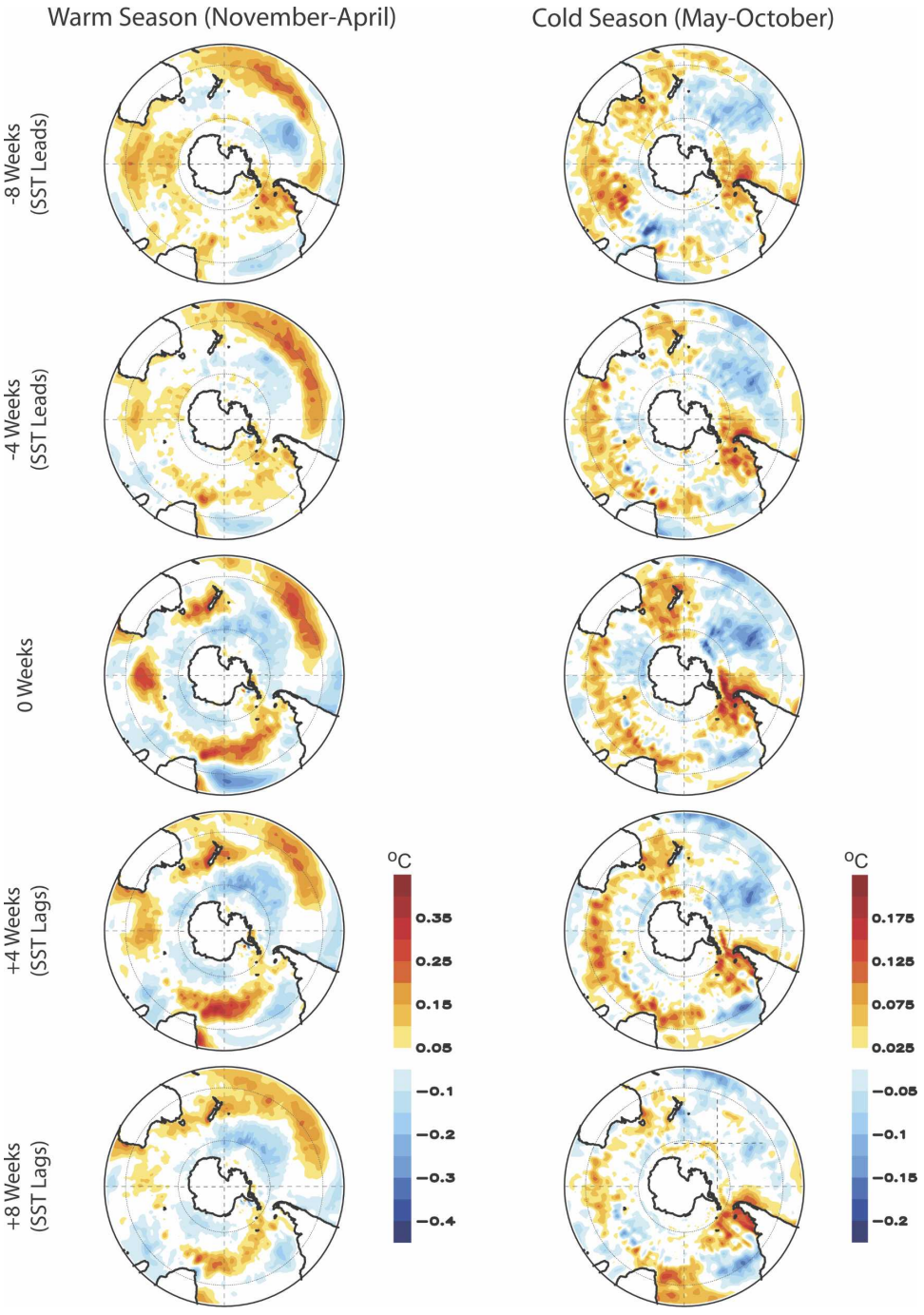

FIG. 6. Weekly (left) warm and (right) cold season SST anomalies regressed on weekly values of the SAM index at (top) lag −8 weeks (SST leads SAM), (second from top) lag −4 weeks, (middle) lag 0 weeks, (second from bottom) lag +4 weeks (SST lags SAM), and (bottom) lag +8 weeks. Note the color scale differs between warm and cold seasons.

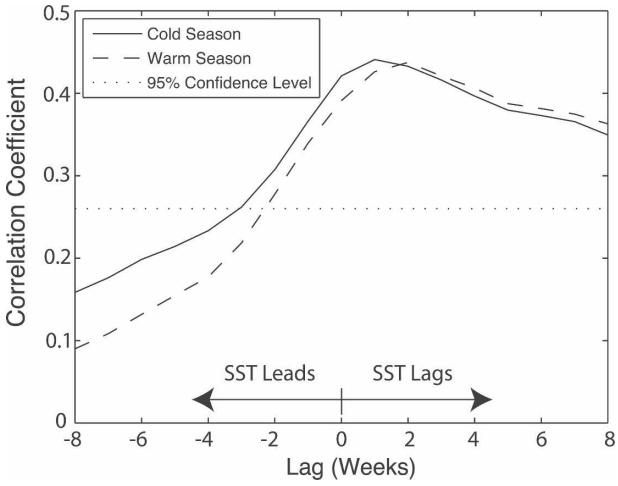

FIG. 7. Lagged correlation coefficients between the SAM index and the expansion coefficient time series of the SST pattern associated with the SAM (i.e., the lag 0 regression maps from Fig. 6) for warm (dashed) and cold (solid) seasons. The 95% confidence level is denoted by the dotted line ($r \sim 0.26$).

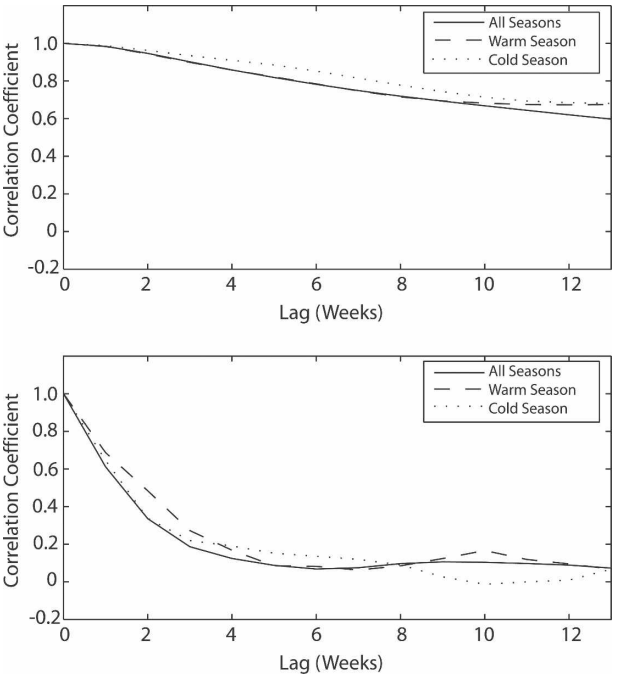

FIG. 8. Lag autocorrelations of (top) the expansion coefficient time series of the SST pattern associated with the SAM (i.e., the lag 0 regression maps from Fig. 6) and (bottom) the SAM index for all seasons (solid) and warm (dashed) and cold (dotted) seasons. See text for details.

relations are weak when SSTs lead by 8 weeks ($r \sim 0.1$) but are still significant when SSTs lag by 8 weeks ($r \sim 0.30$). The slow decay of the lag correlations after lag 0 attests to the substantial persistence of the SH SST field. Note that when SSTs lag the SAM, the magnitude of the correlation coefficients are virtually identical in both seasons, but when SSTs lead the SAM, the correlation coefficients are slightly stronger in the cold season.

The persistence of the SAM and its impact on the SST field is investigated further in Figs. 8–10. The top panel in Fig. 8 shows the lag autocorrelations of the SAM_{SST} time series for the austral warm season (dashed), the austral cold season (dotted), and all seasons (solid) for lags up to 13 weeks (i.e., the length of the cold and warm seasons used in the analyses). The autocorrelation function for the SAM_{SST} time series is repeated for all seasons for lags up to 52 weeks in Fig. 10 (thin solid line). The bottom panel in Fig. 8 shows the seasonally stratified lag autocorrelations for the SAM index time series.

The most obvious feature in the autocorrelation plots in Fig. 8 is the marked persistence of the SAM_{SST} pattern relative to the SAM itself: the *e*-folding time scale of the SAM index is roughly two weeks, whereas the *e*-folding time scale of its expression in the SST field is on the order of 26 weeks (Fig. 10, thin solid line). The SAM_{SST} time series exhibits slightly more persistence during the cold season (Fig. 8, top), whereas the SAM index time series exhibits slightly more persistence during the warm season (Fig. 8, bottom).

As discussed in previous sections, the SAM and ENSO are significantly related during the austral warm season. Thus a fraction of the persistence of the SAM and SAM_{SST} time series during the austral warm season is due to the relatively low-frequency variability inherent in ENSO. Figure 9 is analogous to Fig. 8, but in all cases ENSO has been linearly regressed from the SAM and SAM_{SST} time series before calculating the lag autocorrelations. The persistence of the cold season time series is unchanged between Figs. 8 and 9 consistent with the fact ENSO and the SAM are not related during that season. But the removal of ENSO has a notable impact on the persistence of the SAM_{SST} time series during the warm season and, by extension, across all seasons. In fact, as evidenced in Fig. 10, the *e*-folding time scale of the SAM_{SST} time series for all seasons is reduced from 26 weeks to 18 weeks after ENSO is linearly regressed from the data. Comparing Figs. 8 and 9, it is clear that, when ENSO is removed from the data, the SAM_{SST} pattern exhibits substantially more persistence during the winter months. Note that ENSO accounts for a relatively small fraction of the persistence of the SAM index itself (cf. the dashed lines in the bottom panels of Figs. 8 and 9).

The ENSO-residual SAM_{SST} time series in Fig. 9 may be viewed as reflecting more precisely the direct effect of the SAM on the SST field. Why does the impact of

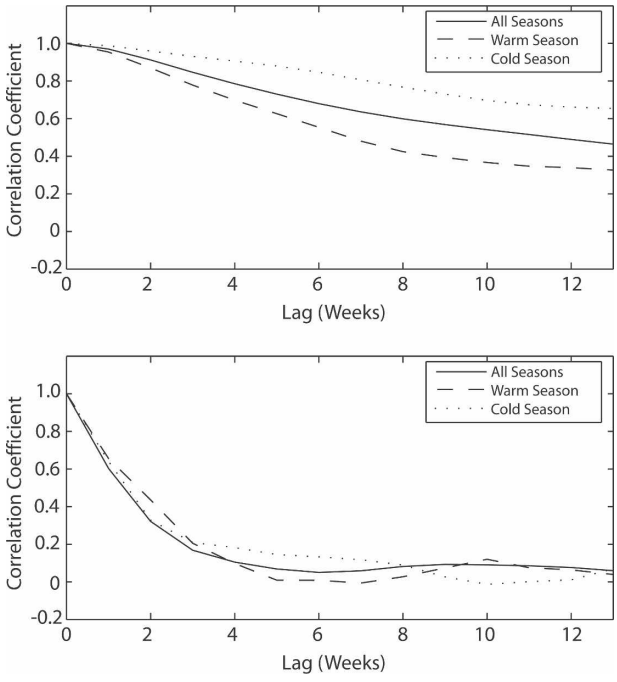

FIG. 9. As in Fig. 8, but ENSO has been linearly regressed from both the SAM index and the expansion coefficient time series of the SST pattern associated with the SAM.

the SAM on the SST field exhibit more persistence during winter despite the fact the atmospheric forcing (i.e., the SAM index) exhibits comparable persistence between seasons? One possible explanation lies in the seasonally varying depth of the ocean mixed layer. The relationship between the mixed layer depth and persistence in SST anomalies can be illustrated in the context of the simple stochastic climate model as described by Frankignoul and Hasselman (1977):

$$\rho c_p H \frac{dT'}{dt} = F' - \lambda T', \tag{2}$$

where ρ and c_p are the density and heat capacity of seawater, respectively; H is the depth of the ocean mixed layer; T' is the anomalous sea surface temperature; λ is a linear damping parameter; and F' is the anomalous atmospheric forcing. If the atmospheric forcing F' is white in time, (2) yields the following autocorrelation function for T':

$$r(\tau) = e^{-\lambda\tau/\rho c_p H}, \tag{3}$$

where $r(\tau)$ is the autocorrelation function of T' as a function of lag (see Frankignoul and Hasselman 1977; Deser et al. 2003). From (3) it is apparent that, all other factors being held equal, the decay time scale of T' decreases exponentially as H increases.

Figure 11 shows solutions to (3) for two different values of mixed layer depths, $H = 35$ m and $H = 90$ m (thick shaded lines), superposed on the cold and warm season lag autocorrelations of the ENSO-residual $\mathrm{SAM}_{\mathrm{SST}}$ time series reproduced from the top panel in Fig. 9 (dashed and dotted lines). When solving for (3), we have set $\rho = 1000$ kg m^{-3} and $c_p = 4218$ J kg^{-1} K^{-1}, and have defined the linear damping parameter as

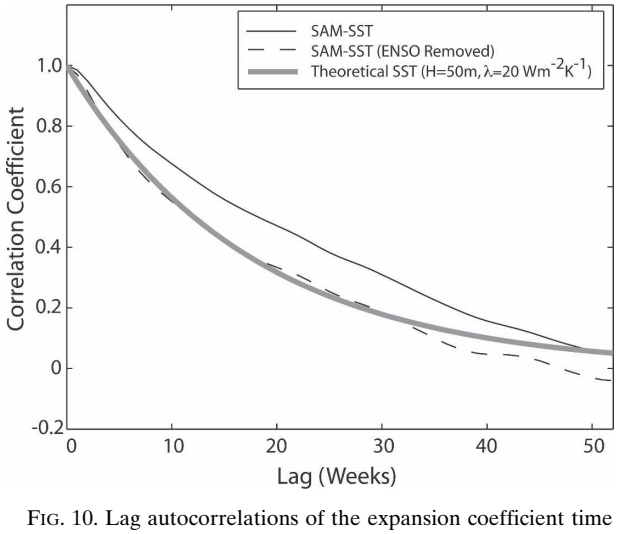

FIG. 10. Lag autocorrelations of the expansion coefficient time series of the SST pattern associated with the SAM for all seasons (thin solid) and for all seasons with ENSO linearly regressed from the data (dashed). The heavy gray shaded line represents the solution to Eq. (3) for $\rho = 1000$ kg m^{-3}, $c_p = 4218$ J kg^{-1} K^{-1}, $\lambda = 20$ W m^{-2} K^{-1}, and a mixed layer depth of $H = 50$ m.

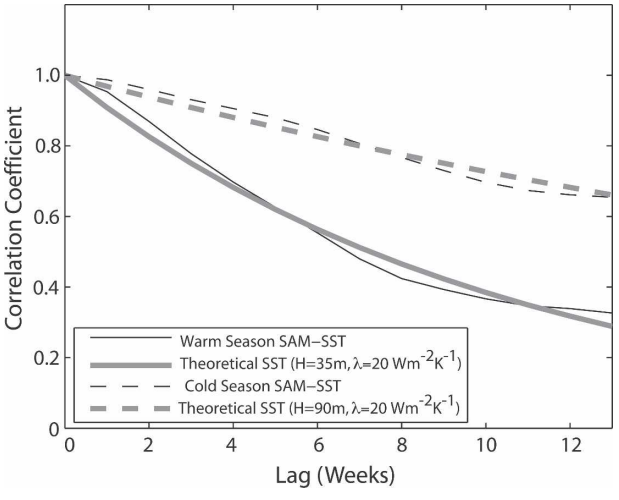

FIG. 11. Lag autocorrelations of the expansion coefficient time series of the SST pattern associated with the SAM for warm (thin solid) and cold (thin dashed) seasons (repeated from Fig. 9, top). The heavy shaded lines represents the solutions to Eq. (3) for $\rho = 1000$ kg m^{-3}, $c_p = 4218$ J kg^{-1} K^{-1}, $\lambda = 20$ W m^{-2} K^{-1}, and mixed layer depths of $H = 90$ m (heavy dashed shading) and $H = 35$ m (heavy solid shading).

$\lambda = 20$ W m^{-2} K^{-1} (20 W m^{-2} represents a rough average value of the damping coefficients used in previous studies of the persistence of the middle latitude oceans; e.g., Deser et al. 2003). The mixed layer depths of $H = 35$ m and $H = 90$ m are chosen because they provide close fits to the observed autocorrelations, but the values also correspond to physically reasonable estimates of the depth of midlatitude SH mixed layer during the warm and cold seasons, respectively [e.g., the hemispheric mean (20°–80°S) mixed layer depths in Fig. 2 are ~50 m during the warm season and ~95 m during the cold season].

The stochastic climate model described in Frankignoul and Hasselman (1977) is a simplification of ocean–atmosphere interaction and neglects several factors that may impact the persistence of extratropical SST anomalies, including, for example, mixed layer dynamics (e.g., Deser et al. 2003), ocean dynamics, forcing of SST anomalies by multiple phenomena (e.g., Newman 2007), and the strength of ocean–atmosphere coupling (e.g., Barsguli and Battisti 1998). However, from Fig. 11 it is clear that physically reasonable differences in the depth of the Southern Ocean mixed layer are sufficient to explain the observed differences in the persistence of the SAM_{SST} time series between warm and cold seasons. A seasonal mean mixed layer depth of 50 m provides a very close fit to the observed persistence of the SAM_{SST} time series based on data for all calendar months (Fig. 10, heavy shaded line).

Note that the calculations in Fig. 11 do not a provide an exact quantification of the impacts of the seasonally varying mixed layer on the persistence of SST anomalies, but rather provide evidence that the persistence of the impact of the SAM on the SST field is consistent with the damp thermal response to relatively high-frequency variability.

5. Summary and conclusions

The analyses presented here support the studies reviewed in the introduction, but also extend those studies by 1) documenting and interpreting seasonal variations in the impact of the SAM and ENSO on the SH extratropical sea surface temperature field, 2) examining the mechanisms through which ENSO and the SAM drive SST variability not only in the vicinity of the ACC but throughout the SH, 3) documenting the observed relationships between the SAM and SH SSTs on week-to-week time scales as a function of season, and 4) providing evidence for and an interpretation of seasonal variations in the persistence of SST anomalies associated with the SAM.

The main conclusions of the study are the following:

1) *The patterns of SST anomalies associated with the SAM and ENSO vary as a function of season in terms of both their structures and their amplitudes.*

   During the cold season, the high index polarity of the SAM is associated with predominantly cold SSTs poleward of 50°S and warm SSTs equatorward of 50°S, except for a large region of cold anomalies that extends from the west of the Antarctic Peninsula to middle latitudes. The cold phase of the ENSO cycle shares with the SAM the large band of negative SST anomalies to the west of the Antarctic Peninsula, but also exhibits pronounced positive SST anomalies in the southern Pacific Ocean.

   During the warm season, the expressions of ENSO and the SAM in the SH SST field bear strong resemblance to each other, consistent with the linear relationship between the SAM and ENSO at that time. Thus, the warm season SAM pattern in SSTs is similar to its cold season counterpart, but includes SST anomalies that extend equatorward toward the tropical Pacific Ocean, and the warm season ENSO pattern in SSTs resembles its cold season counterpart, but includes SST anomalies that extend into the Atlantic and Indian Ocean sectors.

   The amplitudes of the impacts of the SAM and ENSO on the SH SST field are largest during the warm season, consistent with the relatively shallow mixed layer at this time.

2) *The anomalous turbulent heat fluxes associated with the SAM play a key role in generating the observed SST anomalies throughout the SH, while the associated anomalous Ekman heat fluxes are important primarily over high latitudes.*

   A comparison of the structures of the SST, surface turbulent and Ekman heat flux anomalies associated with the SAM suggests the turbulent fluxes play an important role in driving the SAM-related SST anomalies throughout much of the Southern Hemisphere. The results also suggest that anomalous heat advection by Ekman currents plays a key role in the vicinity of the Antarctic Circumpolar Current (ACC), consistent with Verdy et al. (2006), but are of secondary importance elsewhere (e.g., compare Fig. 4, middle and bottom panels). The turbulent heat fluxes exhibit the largest amplitude during the cold season, while the Ekman heat fluxes exhibit comparable amplitude year-round.

   The ENSO-related SH SST anomalies project strongly onto the ENSO-related Ekman heat flux anomalies, but the relationships between the ENSO-related SST and turbulent heat flux anomalies over the SH are less clear.

3) *SST anomalies associated with the SAM are largest roughly one week after large changes in the atmospheric flow and persist for up to six months.*

   The correlations between the SAM and its associated pattern of SST anomalies are strongest and most statistically significant when the SST field lags the SAM by ~1 week and remain significant for lags up to several months. Correlations are much weaker for periods when the SAM lags the SST field, and there is no evidence of a distinct pattern of weekly extratropical SH SST anomalies that precedes variability in the SAM. The observed persistence of the pattern of SST anomalies associated with the SAM in is consistent with the simulated persistence revealed in Sen Gupta and England (2006).

4) *The seasonally varying persistence of the pattern of SST anomalies associated with the SAM is consistent with the seasonally varying depth of the ocean mixed layer.*

   SST anomalies associated with the SAM appear at first glance to have comparable persistence during the cold and warm seasons. However, much of the summertime persistence in SST anomalies associated with the SAM derives from the linear relationship between the SAM and ENSO. When ENSO is linearly regressed from the data, the persistence of the SAM SST anomalies is much less during the warm season than it is during the cold season. The differences in the persistence of the ENSO-residual SST anomalies between the cold and warm seasons is consistent with the seasonal cycle in the depth of the SH ocean mixed layer.

Acknowledgments. The authors thank the two anonymous reviewers for their comments, which improved the manuscript. We also thank Dr. Steve Rintoul for his insightful comments on the manuscript and Drs. James Hurrell, Carolina Vera, and John M. Wallace for helpful discussions of the results. The work was supported by the NSF under Grants ATM-0320959 and ATM-0132190.

REFERENCES

Barsguli, J. J., and D. S. Battisti, 1998: The basic effects of atmosphere–ocean thermal coupling on midlatitude variability. *J. Atmos. Sci.,* **55,** 477–493.

Bretherton, C. S., M. Widmann, V. P. Dymnikov, J. M. Wallace, and I. Bladé, 1999: The effective number of spatial degrees of freedom of a time-varying field. *J. Climate,* **12,** 1990–2009.

de Boyer Montégut, C., G. Madec, A. S. Fischer, A. Lazar, and D. Iudicone, 2004: Mixed layer depth over the global ocean: An examination of profile data and a profile-based climatology. *J. Geophys. Res.,* **109,** C12003, doi:10.1029/2004JC002378.

Deser, C., M. A. Alexander, and M. S. Timlin, 2003: Understanding the persistence of sea surface temperature anomalies in midlatitudes. *J. Climate,* **16,** 57–72.

Frankignoul, C., 1985: Sea surface temperature anomalies, planetary waves, and air-sea feedback in the middle latitudes. *Rev. Geophys.,* **23,** 357–390.

——, and K. Hasselman, 1977: Stochastic climate models. Part II: Application to sea-surface temperature variability and thermocline variability. *Tellus,* **29,** 289–305.

Hall, A., and M. Visbeck, 2002: Synchronous variability in the Southern Hemisphere atmosphere, sea ice, and ocean resulting from the annular mode. *J. Climate,* **15,** 3043–3057.

Holland, M. M., C. M. Bitz, and E. C. Hunke, 2005: Mechanisms forcing an Antarctic dipole in simulated sea ice and surface ocean conditions. *J. Climate,* **18,** 2052–2066.

Hoskins, B. J., and D. J. Karoly, 1981: The steady linear response of a spherical atmosphere to thermal and orographic forcing. *J. Atmos. Sci.,* **38,** 1179–1196.

Karoly, D. J., 1989: Southern Hemisphere circulation features associated with El Niño–Southern Oscillation events. *J. Climate,* **2,** 1239–1252.

——, 1990: The role of transient eddies in low-frequency zonal variations of the Southern Hemisphere circulation. *Tellus,* **42A,** 41–50.

Karsten, R. H., and J. Marshall, 2002: Constructing the residual circulation of the ACC from observations. *J. Phys. Oceanogr.,* **32,** 3315–3327.

Kidson, J. W., 1988: Interannual variations in the Southern Hemisphere circulation. *J. Climate,* **1,** 1177–1198.

——, and J. A. Renwick, 2002: The Southern Hemisphere evolution of ENSO during 1981–1999. *J. Climate,* **15,** 847–863.

Kiladis, G. N., and K. C. Mo, 1998: Interannual and intraseasonal variability in the Southern Hemisphere. *Meteorology of the Southern Hemisphere, Meteor. Monogr.,* No. 49, Amer. Meteor. Soc., 307–336.

Kistler, R., and Coauthors, 2001: The NCEP–NCAR 50-Year Reanalysis: Monthly means CD-ROM and documentation. *Bull. Amer. Meteor. Soc.,* **82,** 247–267.

Lefebvre, W., H. Goosse, R. Timmermann, and T. Fichefet, 2004: Influence of the Southern Annular Mode on the sea ice–ocean system. *J. Geophys. Res.,* **109,** C09005, doi:10.1029/2004JC002403.

L'Heureux, M. L., and D. W. J. Thompson, 2006: Observed relationships between El Niño–Southern Oscillation and the extratropical zonal-mean circulation. *J. Climate,* **19,** 276–287.

Li, Z. X., 2000: Influence of tropical Pacific El Niño on the SST of the Southern Ocean through atmospheric bridge. *Geophys. Res. Lett.,* **27,** 3505–3508.

Lorenz, D. J., and D. L. Hartmann, 2001: Eddy-zonal flow feedback in the Southern Hemisphere. *J. Atmos. Sci.,* **58,** 3312–3327.

Lovenduski, N. S., and N. Gruber, 2005: Impact of the Southern Annular Mode on Southern Ocean circulation and biology. *Geophys. Res. Lett.,* **32,** L11603, doi:10.1029/2005GL022727.

Meredith, M. P., and A. M. Hogg, 2006: Circumpolar response of Southern Ocean eddy activity to a change in the Southern Annular Mode. *Geophys. Res. Lett.,* **33,** L16608, doi:10.1029/2006GL026499.

——, P. L. Woodworth, C. W. Hughes, and V. Stepanov, 2004: Changes in the ocean transport through Drake Passage during the 1980s and 1990s, forced by changes in the Southern Annular Mode. *Geophys. Res. Lett.,* **31,** L21305, doi:10.1029/2004GL021169.

Newman, M., 2007: Interannual to decadal predictability of tropi-

cal and North Pacific sea surface temperatures. *J. Climate*, **20,** 2333–2356.

North, G. R., T. L. Bell, R. F. Cahalan, and F. J. Moeng, 1982: Sampling errors in the estimation of empirical orthogonal functions. *Mon. Wea. Rev.,* **110,** 699–706.

O'Neill, L. W., D. B. Chelton, and S. K. Esbensen, 2003: Observations of SST-induced perturbations of the wind stress field over the Southern Ocean on seasonal timescales. *J. Climate,* **16,** 2340–2354.

Renwick, J. A., 2002: Southern Hemisphere circulation and relations with sea ice and sea surface temperature. *J. Climate,* **15,** 3058–3068.

Reynolds, R. W., and T. M. Smith, 1994: Improved global sea surface temperature analysis using optimum interpolation. *J. Climate,* **7,** 929–948.

——, N. Rayner, T. M. Smith, D. C. Stokes, and W. Wang, 2002: An improved in situ and satellite SST analysis for climate. *J. Climate,* **15,** 1609–1625.

Sardesmukh, P. D., and B. J. Hoskins, 1988: The generation of global rotational flow by steady idealized tropical divergence. *J. Atmos. Sci.,* **45,** 1228–1251.

Sen Gupta, A., and M. H. England, 2006: Coupled ocean–atmosphere–ice response to variations in the Southern Annular Mode. *J. Climate,* **19,** 4457–4486.

Thompson, D. W. J., and J. M. Wallace, 2000: Annular modes in the extratropical circulation. Part I: Month-to-month variability. *J. Climate,* **13,** 1000–1016.

Verdy, A., J. Marshall, and A. Czaja, 2006: Sea surface temperature variability along the path of the Antarctic Circumpolar Current. *J. Phys. Oceanogr.,* **36,** 1317–1331.

Watterson, I. G., 2000: Southern midlatitude zonal wind vacillation and its interaction with the ocean in GCM simulations. *J. Climate,* **13,** 562–578.

Woodruff, S. D., R. J. Slutz, R. L. Jenne, and P. M. Steurer, 1987: A comprehensive ocean-atmosphere data set. *Bull. Amer. Meteor. Soc.,* **68,** 1239–1250.